ADVANCED MATERIALS
www.advmat.de

2D Molybdenum Disulfide Embedded Photonic Crystal Fiber for all-Fiber Phase Retarder

Ding Zhong, Jiajie Gan, Jiantao Peng, Guodong Xue, Zhiwei Liang, Quanlin Guo, Yu Fu, Xinyao Shan, Han Dong, Xu Cheng, Wentao Yu, Yonggang Zuo, Xin Jiang, Kaihui Liu, Zhongfan Liu,* Xu Zhou,* and Can Liu**

The integration of 2D materials with optical fibers enables multifunctional fiber devices, such as polarizers, modulators, and sensors. Recent advances in direct vapor deposition growth further enhance light-2D material interactions to centimeter-scale lengths, overcoming the micrometer-scale limitations of transferred 2D materials. However, conventional methods for growing 2D materials in fibers typically produce isotropic material architectures due to uniform precursor deposition, limiting applications that require birefringence, such as a phase retarder. Here, a selective vapor deposition method is proposed to realize the non-circular symmetric growth of 2D molybdenum disulfide (MoS_2) into photonic crystal fibers (PCFs), achieving anisotropy-engineered phase retardation. The high refractive index of MoS_2 efficiently breaks the degeneracy of polarization modes in PCF and enables phase retardation with a manageable beat length of ≈7.7 cm. The MoS_2-PCF phase retarder reliably works in varying conditions, including outdoor exposure, large deformation, and high temperature/humidity. Its phase retardation exhibits an extremely small fluctuation of ≈3.3° between 25 and 200 °C, which is two orders of magnitude lower than that of commercial polarization-maintaining fibers (≈2.0°/°C). The work provides a new solution for the fiber device preparation and pave the way for robust polarization manipulation in all-fiber systems.

1. Introduction

2D materials, with their valley-selective absorption,[1,2] tunable optical properties,[3–5] and exceptional optical nonlinear effect,[6,7] hold great promise for light manipulation, such as polarized light control, high-speed optical switching, and nonlinear frequency conversion.[7–9] Nevertheless, their atomic thickness inherently restricts light-matter interaction length, which limits the effectiveness of light manipulation, e.g., weak saturable absorption process for ultrafast lasers, low efficiency for frequency conversion. To enhance the light-2D materials interaction, great efforts have been devoted to integrating 2D materials with waveguides, particularly optical fibers, which have demonstrated multifunctional capabilities.[10–13] For instance, transferring 2D materials onto tapered fibers, D-shaped fibers, or fiber endfaces has enabled applications of passive mode-locking, optical parametric conversion, and electrically controllable

D. Zhong, Y. Fu, X. Shan, C. Liu
Key Laboratory of Quantum State Construction and Manipulation (Ministry of Education)
School of Physics
Renmin University of China
Beijing 100872, China
E-mail: canliu@ruc.edu.cn

D. Zhong, J. Gan, J. Peng, Z. Liang, X. Zhou
Basic Research Centre of Excellence for Structure and Fundamental Interactions of Matter
Guangdong Provincial Key Laboratory of Quantum Engineering and Quantum Materials
School of Physics
South China Normal University
Guangzhou 510006, China
E-mail: xuzhou2020@m.scnu.edu.cn

J. Gan, J. Peng, Z. Liang, X. Zhou
Guangdong-Hong Kong Joint Laboratory of Quantum Matter
Frontier Research Institute for Physics
South China Normal University
Guangzhou 510006, China

G. Xue, Q. Guo, K. Liu
State Key Laboratory for Mesoscopic Physics
Frontiers Science Center for Nano-optoelectronics
Academy for Advanced Interdisciplinary Studies
School of Physics
Peking University
Beijing 100871, China
E-mail: khliu@pku.edu.cn

Q. Guo, K. Liu
Interdisciplinary Institute of Light-Element Quantum Materials and Research Centre for Light-Element Advanced Materials
Peking University
Beijing 100871, China

H. Dong, X. Jiang
Russell Centre for Advanced Lightwave Science
Shanghai Institute of Optics and Fine Mechanics and Hangzhou Institute of Optics and Fine Mechanics
Hangzhou 311421, China

The ORCID identification number(s) for the author(s) of this article can be found under https://doi.org/10.1002/adma.202504464

DOI: 10.1002/adma.202504464

polarizers.[14–19] However, the size of the transferred 2D materials is inherently limited to the micrometer scale, restricting their scalability for large-scale applications.

The direct growth approach fundamentally overcomes this scalability limitation by in situ depositing 2D materials along centimeter-scale fiber holes.[20–23] This strategy has enabled MoS_2 integration in microstructured fibers, demonstrating enhanced nonlinear coefficients for supercontinuum generation[24] and significant saturable absorption for mode-locked lasers.[25] However, such progress has been largely confined to applications requiring isotropic light-matter interaction. While targeting polarization-sensitive functionalities like an all-fiber phase retarder, the intrinsic structural symmetry imposed by conventional vapor deposition becomes detrimental. Specifically, the uniform precursor mass flow in vapor deposition processes leads to conformal material coatings that preserve the original circular symmetry of the fiber. To attain the necessary birefringence for polarization manipulation of photons, controls over material architecture, such as selective hole filling ratios, symmetry breaking in material distribution, and position-specific deposition, must be achieved at sub-micron precision. However, such selective growth demands independent precursor flux modulation across individual micron-scale fiber holes, a feat that current deposition systems cannot accomplish due to their intrinsic lack of spatial resolution at the fiber-hole-array level.

Here, we proposed a selective vapor deposition method to realize the non-circular symmetric growth of 2D molybdenum disulfide (MoS_2) into isotropic photonic crystal fibers (PCFs). MoS_2 is deliberately selected as the filling layer since its high refractive index can significantly break the isotropic structure of PCF, inducing an effective birefringence,[26,27] and its atomically thin thickness does not alter the intrinsic transmission characteristics.[28] By pre-depositing Mo precursors in a row of holes of the PCF and subsequently subjecting it to high-temperature sulfurization, an anisotropic material architecture within the fiber was successfully achieved. This design enables the MoS_2-PCFs to serve effectively as all-fiber phase retarders without disrupting the propagation modes. In addition, the minimal variation of MoS_2's refractive index with temperature,[29] together with its flexible properties,[30,31] endows our phase retarder with enhanced stability against external heat and mechanical stresses. Our strategy provides an alternative route for material-induced birefringence beyond the stress- or geometry-based approaches.

X. Cheng
Group for Fibre Optics
École Polytechnique Fédérale de Lausanne (EPFL)
Lausanne 1015, Switzerland

W. Yu
Institute of Interdisciplinary Physical Sciences
School of Physics
Nanjing University of Science and Technology
Nanjing 210094, China

Y. Zuo
Faculty of Metallurgical and Energy Engineering
Kunming University of Science and Technology
Kunming 650093, China

Z. Liu
College of Chemistry and Molecular Engineering
Peking University
Beijing 100871, China
E-mail: zfliu@pku.edu.cn

Z. Liu
Beijing Graphene Institute (BGI)
Beijing 100095, China

2. Results and Discussion

2.1. Selective Growth of MoS_2 in PCFs

In our experiment, a selective vapor deposition method was developed to fabricate MoS_2 films into certain holes of single-mode PCFs (**Figure 1a**). First, a pair of parallelly aligned 100-nm-thick Au strips was transferred onto the end face of a bare PCF, only leaving the middle row of holes along the *y*-direction exposed (Figure S1, Supporting Information). The partially hole-blocked PCF was then filled with Na_2MoO_4 aqueous solution by capillarity, leading to the pre-deposition of Mo sources in the exposed holes. Subsequently, the fiber was dried and loaded into a chemical vapor deposition (CVD) furnace for MoS_2 growth. At the growth temperature of 800 °C, the pre-filled Na_2MoO_4 volatilized and then deposited into the inner walls of the fiber as uniformly distributed small molten droplets. After sulfuration by a sufficient sulfur vapor supply at low pressure, MoS_2 films were uniformly deposited within the selected middle row of holes along the *y*-direction. The uniform length of the MoS_2-PCF was significantly impacted by the concentration of Na_2MoO_4 aqueous solution, which was optimized as 70 mg mL^{-1} for embedding growth of monolayer MoS_2 (Figure S2, Supporting Information). Based on this optimized condition, we achieved the uniform growth of tubular monolayer MoS_2 throughout a length exceeding 10 cm within the PCF (Figures S3 and S4, Supporting Information).

The selective growth of MoS_2 is facilely confirmed utilizing an optical microscope while capturing side views from different directions. When focusing along the *x*-direction, a uniform green contrast of all MoS_2-embedded holes was in sight (Figure 1b), whereas only one row was in the focal plane along the *y*-direction (Figure 1c). The photoluminescence (PL) spectrum collected from the selected fiber hole exhibited the typical A exciton peak located ≈670 nm, indicating the monolayer feature of as-grown MoS_2 (Figure 1d). The frequency difference between the A_{1g} and E_{2g} Raman modes was extracted as ≈19 cm^{-1} (Figure 1e), a characteristic frequency difference of monolayer MoS_2.[32,33] A slight redshift of E_{2g} mode compared to that on a flat silica substrate was observed, attributed to the tube-like geometry of MoS_2 embedded in the inner walls of the fiber (Figure S5, Supporting Information).[34] The Raman mapping of E_{2g} mode intensity in the outlined area of Figure 1c further demonstrated the large-scale uniformity of the selectively deposited MoS_2 films (Figure 1f). To precisely characterize the quality of MoS_2 layers, the silica walls of PCF were etched off, leaving isolated tube-like MoS_2 (Figure S6, Supporting Information and Experimental Section). A clear moiré pattern of the collapsed MoS_2 tube was visualized in the scanning transmission electron microscopic (STEM) image (Figure 1g), demonstrating the high crystallinity of as-grown MoS_2 films. The uniformly embedded high-quality MoS_2 monolayers within selective holes impart phase manipulation functionality to the MoS_2-PCF and facilitate its subsequent performance evaluations.

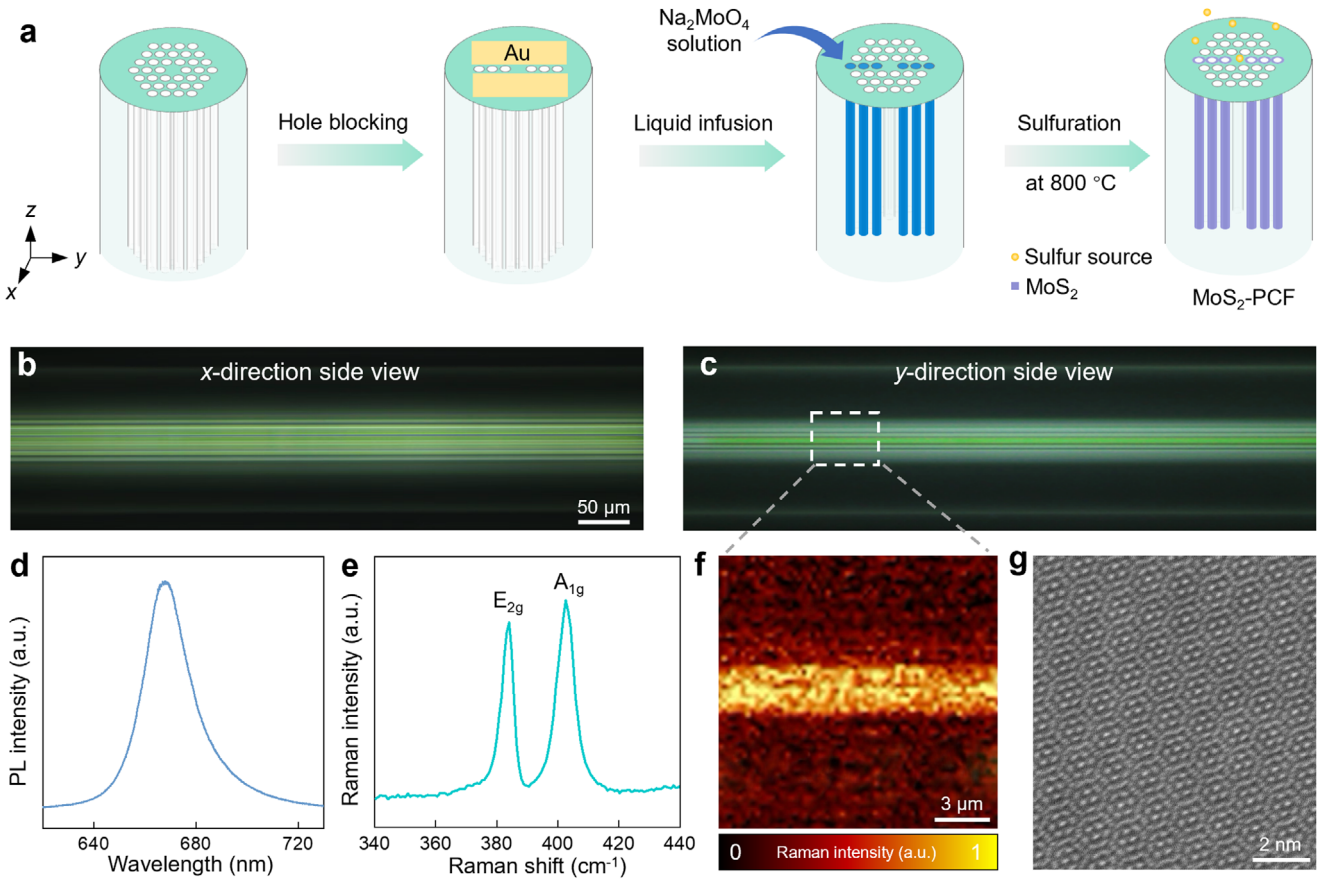

Figure 1. Fabrication and characterization of MoS_2-PCFs. a) Schematic of the selective growth of MoS_2 in PCFs, which involves partially blocking holes with Au strips; infusing Na_2MoO_4 aqueous solution into PCFs; and sulfuration at a high temperature. b,c) Optical image of a MoS_2-PCF in the *x*-direction (b) and *y*-direction side view (c), respectively, indicating MoS_2 was selectively grown only along the row of holes in the *y*-direction of the PCF. d,e) PL (d) and Raman (e) spectra of the MoS_2 embedded in PCF. f) Raman mapping based on the E_{2g} mode intensity in the outlined area of (c), verifying the selective growth of MoS_2 in PCF. g) STEM image of collapsed MoS_2 strip transferred onto a hollow grid, revealing its high crystallinity.

2.2. Utilization of MoS_2-PCFs as Phase Retarders

To evaluate the phase manipulation effect of MoS_2 layers, 1550 nm-light propagation modes in MoS_2-PCF (with monolayer MoS_2 selectively embedded into the middle row of holes along the *y*-direction) were studied using the full-vector finite element method (**Figure** 2a,b). The light field (*E*) profile of fundamental mode HE_{11} after embedding MoS_2 showed that the light remained primarily confined within the fiber core, suggesting that MoS_2 films do not destroy the propagation mode of the PCF and thus preserve the signal transmission (Figure 2c). In addition, the light intensities of the two orthogonal modes HE_{11}^{x} and HE_{11}^{y} were not completely overlapping, verifying that these originally degenerate two fundamental modes become nondegenerate after MoS_2 is embedded (Figure 2d). Moreover, a distinct *E* saltation of HE_{11}^{y} was observed at the interfaces of silica/MoS_2/air in the *y*-direction, arising from their sudden change of refractive indices (1.44, 3.65, and 1.00 for silica, MoS_2, and air, respectively), which significantly affects the HE_{11}^{y} light transmission characteristics due to the strong light-MoS_2 interaction.[21] Notably, such a saltation was not observed in the *x*-direction (Figure S7, Supporting Information). The simulated effective refractive index of HE_{11}^{y} was lower than that of HE_{11}^{x}, leading to a larger propagation velocity of *y*-polarized light (Figure S8, Supporting Information). Therefore, phase retardation between HE_{11}^{x} and HE_{11}^{y} light was involved, altering the polarization state of the output light.

The calculated birefringence and beat length (L_p) of MoS_2-PCF were $\approx 2.2 \times 10^{-5}$ and ≈7.2 cm, respectively (Figure 2e and Experimental Section). To reach the same birefringence, it requires a much greater thickness of ≈24.3 nm for SiO_2, stemming from the fact that monolayer MoS_2 can locally confine more optical field energy and highlighting the advantages of monolayer MoS_2 (thickness of ≈0.7 nm) as a filling material for modulating the optical birefringence (Figure S9, Supporting Information). Furthermore, the manageable beat length of MoS_2-PCF facilitates easier splicing and integration with an all-fiber system as it reduces the sensitivity of phase retardation to fiber length variations, thereby improving the stability and control of the polarization state.

2.3. Phase Manipulation Capability of MoS_2-PCFs

To investigate the phase manipulation capacity of MoS_2-PCFs, we employed a methodology based on Mueller matrix and Stokes

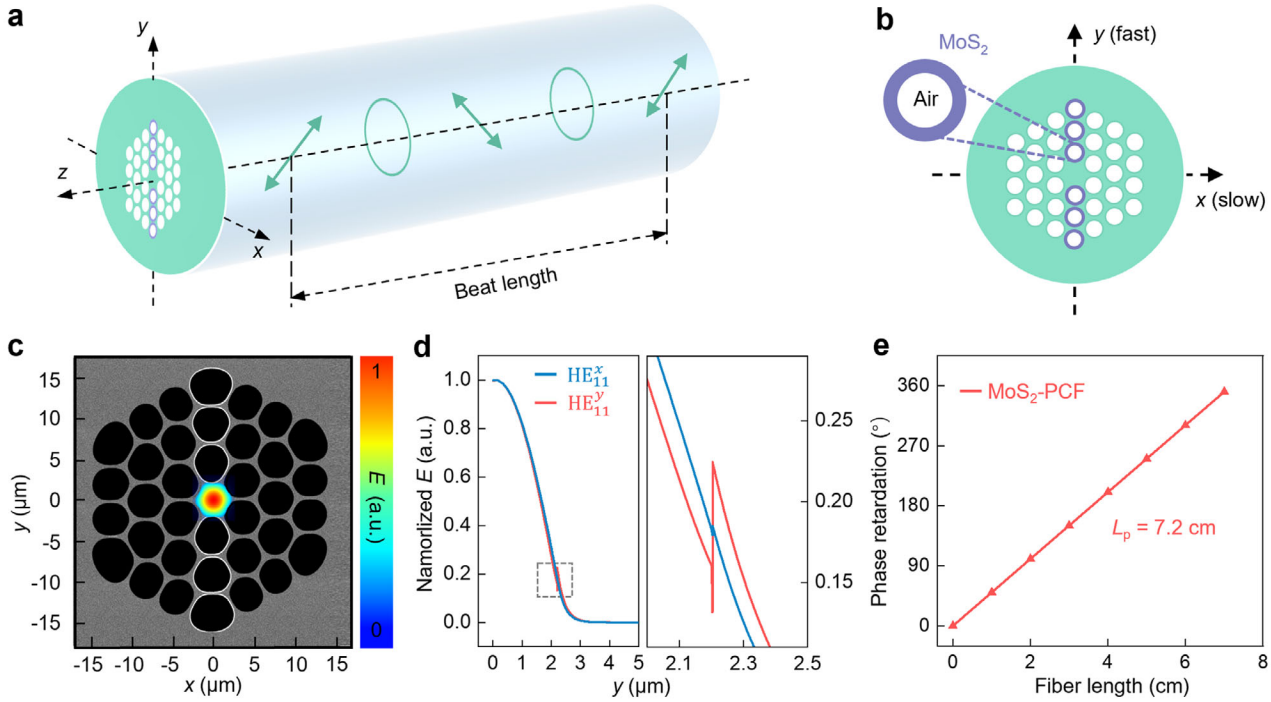

Figure 2. Phase manipulation of MoS_2-PCFs. a) Schematic of the MoS_2-PCF phase retarder. MoS_2 was selectively embedded only along the row of holes passing through the core in the *y*-direction of the PCF, inducing material birefringence and phase retardation. The periodic variation in the polarization state corresponds to the beat length. b) Schematic of the end face of the phase retarder. The selective embedded MoS_2 made the *y*-axis the fast axis. c) Optical field (*E*) profile of HE_{11} mode in the 4.35 μm-core PCF embedded with monolayer MoS_2 at the wavelength of 1550 nm. d) Normalized electric *E* distribution of the HE_{11}^{x} (blue curve) and HE_{11}^{y} (red curve) in the *y*-direction of (c). Right, zoomed-in view of the dashed square in the left panel, showing a distinct saltation. e) The simulated phase retardation of MoS_2-PCF with different lengths. The beat length L_p was extracted as 7.2 cm.

vector analyses[35,36] (**Figure 3a**). Assuming a known polarized light with Stokes vector $\boldsymbol{S}_{in}$ incident upon a sample, the generated Stokes vector $\boldsymbol{S}_{out}$ containing sample characteristic information can be obtained as:

$$\boldsymbol{S}_{out} = \begin{bmatrix} S_0 \\ S_1 \\ S_2 \\ S_3 \end{bmatrix} = \boldsymbol{M}_s \, \boldsymbol{S}_{in} = \begin{bmatrix} 1 & 0 & 0 & 0 \\ 0 & m_{22} & m_{23} & m_{24} \\ 0 & m_{32} & m_{33} & m_{34} \\ 0 & m_{42} & m_{43} & \cos\eta_s \end{bmatrix} \begin{bmatrix} \hat{S}_0 \\ \hat{S}_1 \\ \hat{S}_2 \\ \hat{S}_3 \end{bmatrix} \quad (1)$$

Here, $\boldsymbol{M}_s$ is the Mueller matrix of the sample, m_{ij} (i = 2, 3,4 and j = 2, 3, 4) are the nonzero elements of the Mueller matrix, and η_s is the phase retardation of light after transmitting through the sample. In our experiment, a right-circularly polarized light ($\boldsymbol{S}_{in} = [1\ 0\ 0\ 1]^T$) was incident upon the MoS_2-PCF, and according to Equation (1), we can obtain:

$$\eta_s = \arccos\left(S_3\right) \quad (2)$$

Since the relationship between S_3 and $\boldsymbol{S}_{out}$ can be represented on a Poincaré sphere (Figure 3b), therefore, the phase retardation η_s can be computed by measuring $\boldsymbol{S}_{out}$.

As shown in Figure 3c, by collecting the mode field distribution through an optical beam profiler, only a fundamental mode was transmitted in our MoS_2-PCF, which ensures the accuracy of our phase retardation measurements without considering the disruption of high-order transmission modes. To evaluate the potential transmission loss introduced by MoS_2, we compared the output power transmitted through a 5.5-cm bare PCF and the MoS_2-PCF under identical coupling conditions. The result showed that the MoS_2 coating introduces only ≈2% additional insertion loss due to the weak optical absorption of MoS_2 at 1550 nm (Table S1, Supporting Information).

The phase retardation of a segment of MoS_2-PCF was measured using a polarimeter, and the L_p of ≈ 7.7 cm was derived from the proportionality between phase retardation and fiber length (Figure 3d and Experimental Section). Note that the small variation from our theoretical predictions arises from inherent fluctuations in the hole geometry. In addition, the nearly perfect linear profile indicates the uniform birefringence in MoS_2-PCF induced by asymmetrically embedded MoS_2 films. The manageable beat length of the MoS_2-PCF facilitates precise cleaving for phase retarders with specific polarization conversion capabilities. Half-wave and quarter-wave retarders were fabricated from MoS_2-PCF with varying lengths, demonstrating that the MoS_2-PCF phase retarder can function as feasibly as that of traditional waveplates (Figure S10, Supporting Information).

2.4. Outstanding Stability Under Various Environmental Conditions

The MoS_2-PCF phase retarder demonstrated excellent stability under outdoor exposure, large deformation, and high

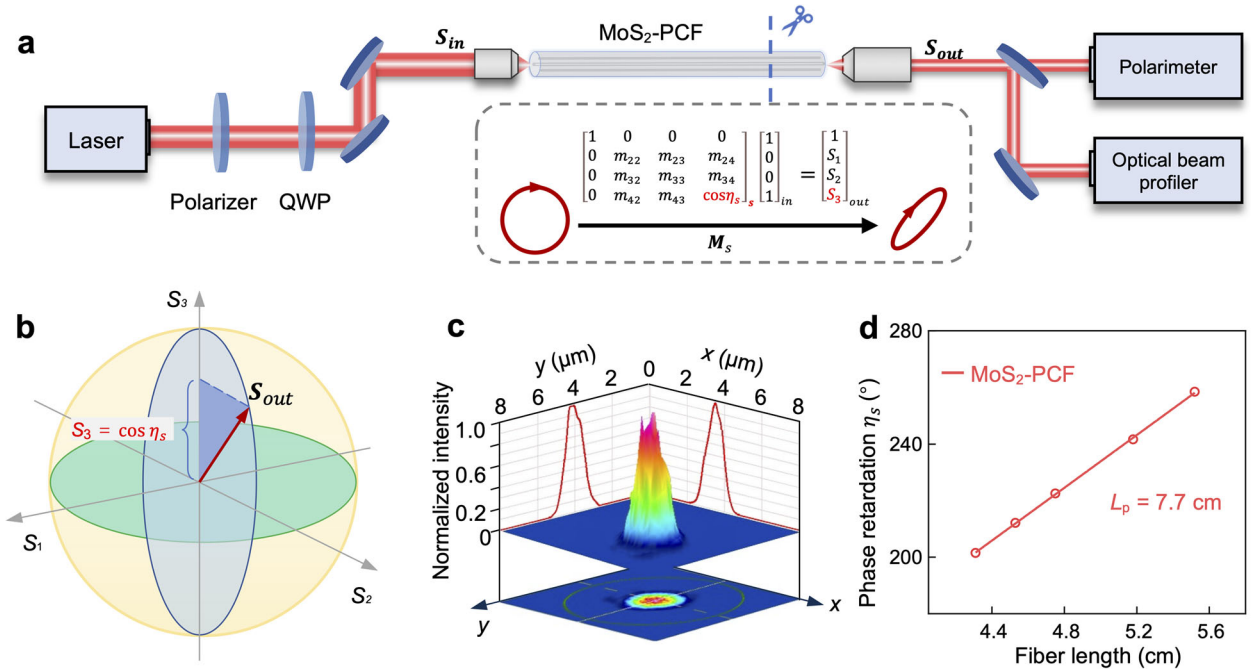

Figure 3. Phase retardation measurement of MoS_2-PCF phase retarder. a) Schematic of the phase retartation measuring system. The optical components consist of a laser, polarizer, quarter-wave plate (QWP), MoS_2-PCF, polarimeter, optical beam profilers, and several reflectors. Circularly polarized light with a wavelength of 1550 nm is transformed into elliptically polarized light after passing through the MoS_2-PCF. b) Schematic of the relationship between the component S_3 and the $\boldsymbol{S}_{out}$ on the Poincaré sphere. c) The normalized intensity distribution of the output beam spot from MoS_2-PCF. The output mode pattern indicates that only the fundamental mode is transmitted. d) Phase retardation (η_s) variation with the length of MoS_2-PCF, featuring a beat length of ≈7.7 cm. The phase retardation of the incident light was set as 0.

temperature/humidity. As illustrated in **Figure** 4a, a 3.7-cm MoS_2-PCF exhibited minimal fluctuation in phase retardation, ranging from +1.2° to −2.1° over the temperature range of 25–200 °C. In contrast, the commercial polarization-maintaining fiber (PMF) displayed significant temperature-dependent phase variation, with phase retardation increasing linearly with temperature (≈2.0°/°C), further highlighting the thermal stability of our MoS_2-PCF. Additionally, the zero-order quarter-wave retarder fabricated from MoS_2-PCF maintained a stable linearly polarized output across varying temperatures when incident upon right-circularly polarized light, confirming its stability of polarization conversion (Figure 4b). Moreover, a small variation of 0.1 cm in retarder length can produce a steady phase change of ≈5° across temperature variations, demonstrating the high sensitivity and robust reliability of phase manipulation, as shown in Figure 4c. The MoS_2-PCF also exhibited bending stability comparable to high-birefringent PMF. When the MoS_2-PCF was bent along the *y*-direction, it showed only 3°-phase-retardation variations across a stress radius range from 10 to 5 cm, arising from the strong structural stability of PCF and excellent mechanical flexibility of MoS_2 (Figure 4d). Furthermore, the retardation fluctuation remained within ±0.3° even when the MoS_2-PCF was exposed to sunlight and relative humidity levels exceeding 90% for 100 h, demonstrating its reliability for both indoor and outdoor conditions (Figure 4e). Given the performance of our MoS_2-PCF, with minimal phase variation under mechanical stress, high humidity, and a wide temperature range, it meets the typical standards for commercial phase retarders, making it highly suitable for integration with all-fiber systems.

3. Conclusion

In summary, we have successfully grown MoS_2 non-circular-symmetrically into specific holes of PCFs through a selective vapor deposition method. Our MoS_2-PCF exhibits uniform birefringence and features a beat length of ≈7.7 cm, ensuring stable polarization conversion while preserving signal transmission. It has exceptional stability against external heat and mechanical stress, and maintains high performance in outdoor environments. The universality of this spatially controlled growth approach enables extension to other 2D materials and complex hole patterns, opening new possibilities for designing fiber devices with tailored anisotropic responses, such as tunable circular-polarization converters, electrically controlled phase retarders, and light emitters with tunable polarization states.

4. Experimental Section

Partially Blocking of PCF's Holes with Au Strips: The PCF was blocked by a well-controlled dry-transfer technique. The polypropylene carbonate (PPC) film was first spin-coated on 100-nm-thick Au strips (patterned by electron-beam lithography) and then peeled off for hole blocking. A piece of PCF was vertically fixed under a microscope, while the Au strip attached to the PPC film was horizontally positioned on a multi-dimensional transfer stage. It was crucial to align the fast axis of the PCF parallel to the edge of the Au strip before advancing the PCF to touch the Au strip. Upon the appearance of Newton rings in the microscope's view, heat was applied to attach the Au strip to the PCF's end face. This blocking process was repeated to cover the other side of the holes by the Au strip. The PPC was removed by annealing at 300 °C for 8 h under a low-pressure condition (<200 Pa) with Ar (500 sccm) and H_2 (50 sccm) flow.

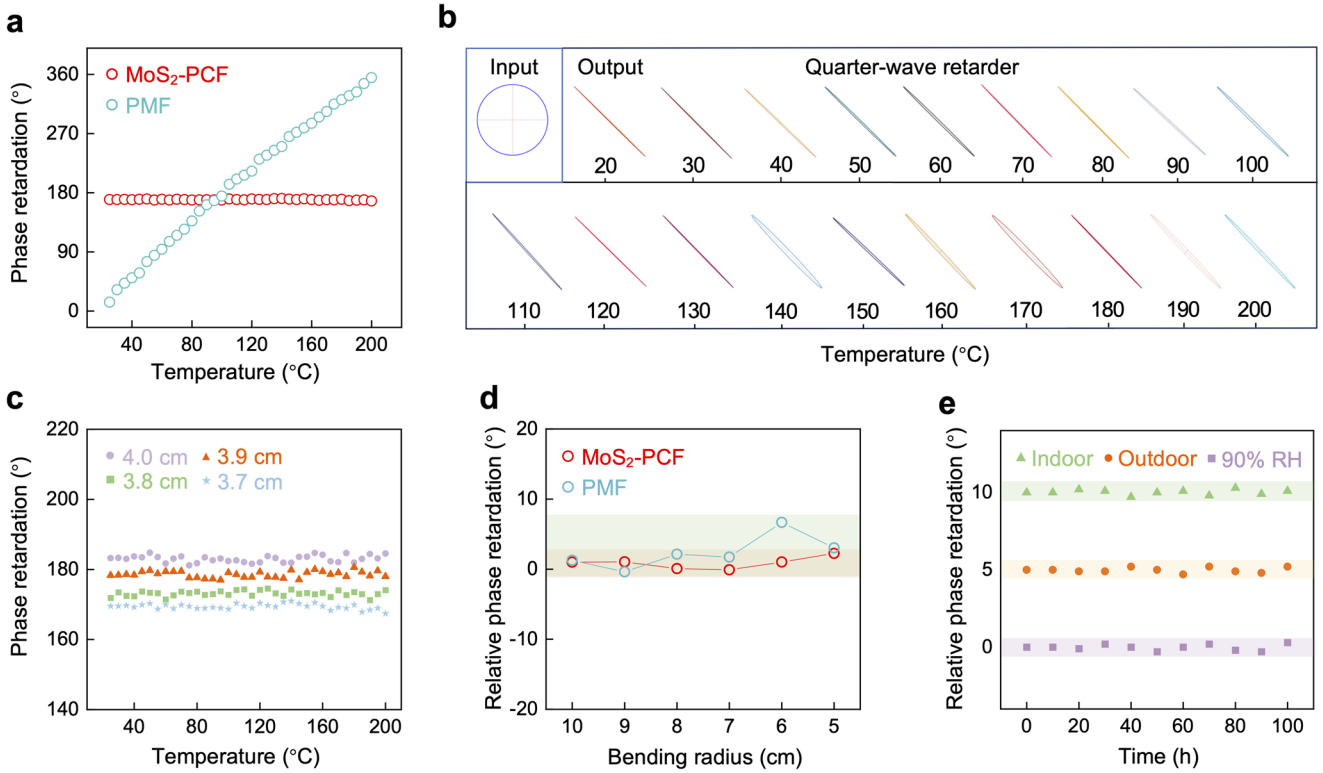

Figure 4. Stability performance of MoS_2-PCF phase retarder. a) Phase retardation of a 3.7-cm MoS_2-PCF and PMF working at 25 to 200 °C. b) The output light characteristics of a quarter-wave retarder fabricated from MoS_2-PCF with circularly polarized input at different temperatures. c) Phase retardation of MoS_2-PCF at varying lengths and temperatures. d) Relative phase retardation in MoS_2-PCF and PMF under different bending radius. e) Variation of phase retardation under indoor, outdoor, and relative humidity greater than 90%. The phase retardation of the incident light was set as 0. The relative phase retardation was shifted vertically for clarity.

Fabrication of MoS_2-PCFs: A single-mode PCF with small silica solid-core (≈4.35 µm) and seven arrays of patterned air-holes was used for the growth of monolayer MoS_2. The Na_2MoO_4 aqueous solution with a required concentration of 70 mg mL^{-1} was filled into the fiber by capillary. Then the feedstock-filled fiber was baked at 110 °C for dewetting, and the pre-deposited fiber was then placed in a CVD furnace, and 1 g sulfur powder (99%, Sigma–Aldrich) was positioned in the upstream region outside the heating zone. The furnace temperature was ramped up to the optimized temperature of ≈800 °C for MoS_2 growth, with an Ar flow of 100 sccm, under 150 Pa. The reduced-pressure environment was essential for enabling uniform sulfur diffusion through the PCF's holes. During the growth, the temperature for sulfur vaporization was maintained at ≈150 °C by a heating belt. After 30 min of growth, the system was naturally cooled down to room temperature.

Isolation of MoS_2 From PCF: The MoS_2-PCF was placed onto a silicon substrate and then immersed in hydrofluoric acid solution (40% in water) for ≈4 h at room temperature. The SiO_2 walls were etched off, and the resulting tube-like MoS_2 monolayers collapsed as strips onto the substrate.

Numerical Modeling: Numerical simulations were processed using the RF module of COMSOL Multiphysics. The effective refractive index of the fundamental guiding mode in MoS_2-PCF was calculated by using the finite element method in COMSOL, and then the beat length can be calculated by $L_P = \lambda/B$. λ is the light wavelength and $B = |Re(n_{eff}^x) - Re(n_{eff}^y)|$ is the fiber birefringence coefficient, where n_{eff}^x and n_{eff}^y is the effective refractive index of the fundamental mode of PCF in the *x*- and *y*- polarization directions, respectively.

Phase Retardation Measurements: A C-band tunable laser (Thorlabs, TLX1) provided a wavelength-tunable CW laser (1550 nm, 10 mW), and then it was transmitted through a polarizer (Thorlabs, LPIREA050-C) and a quarter-wave plate (Thorlabs, WPQ05M-1550) to obtain circularly polarized light. The light was then focused onto the MoS_2-PCF via a lens (Thorlabs, N414TM-C, f = 3.3 mm, NA = 0.47). The signal was collimated by a 40× objective and collected by a polarimeter (Thorlabs, PAX1000IR2/M) and an optical beam profiler (Dataray, BladeCam2-HR). After measuring the phase retardation of a segment of MoS_2-PCF, a portion of this fiber was cut, and then the phase retardation of the remaining segment was measured. The L_P was extracted by continuously cutting different lengths of fiber and measuring their phase retardation. To study its environmental stability, the phase retardation was measured every 10 h of sunlight or relative humidity (RH) exceeding 90% exposure.

Characterizations: Optical images were taken with an Olympus BX51M microscope. Raman and PL measurements were performed using a WITec alpha300R system with a laser excitation wavelength of 514 nm and a power of ≈1 mW. AFM image was obtained using an Asylum Research Cypher AFM system. SEM images were collected by a FEI Nova NanoSEM 430 scanning electron microscope. STEM image was performed in the FEI Titan Themis G2 300 operated at 300 kV.

Supporting Information

Supporting Information is available from the Wiley Online Library or from the author.

Acknowledgements

This work was supported by the National Natural Science Foundation of China (52322205, 52250398, 12274456, 52025023, 52372046, 52203331),

National Key R&D Program of China (2022YFA1405600, 2024YFA1409700, 2022YFA1403500), and Beijing Municipal Science and Technology Project (Z221100005822003) for this work. This work has been supported by the New Cornerstone Science Foundation through the XPLORER PRIZE. The authors acknowledge the iFiber Optoelectronics Technology Co., Ltd. for providing the PCFs.

Conflict of Interest

The authors declare no conflict of interest.

Author Contributions

D.Z., J.G., J.P., and G.X. contributed equally to this work. C.L., X.Z., Z.L. and K.L. conceived the experiments and supervised the project. D.Z. and G.X. contributed to the fabrication of MoS_2-PCFs. J.G., D.Z., Z.L. and H.D. performed the optical experiments. J.P. contributed to the theoretical modelling. Q.G. conducted the STEM experiments. Y.F., X.S., C.X., W.Y., Y.Z. and X.J. helped with the sample characterizations and data analysis. All the authors discussed the results and wrote the manuscript.

Data Availability Statement

The data that support the findings of this study are available in the supplementary material of this article.

Keywords

2D material fiber, birefringence modulation, phase retarder, selective growth

Received: March 6, 2025
Revised: June 12, 2025
Published online:

[1] K. F. Mak, D. Xiao, J. Shan, *Nat. Photon.* **2018**, *12*, 451.
[2] A. Rycerz, J. Tworzydło, C. Beenakker, *Nat. Phys.* **2007**, *3*, 172.
[3] G. Grosso, H. Moon, B. Lienhard, S. Ali, D. K. Efetov, M. M. Furchi, P. Jarillo-Herrero, M. J. Ford, I. Aharonovich, D. Englund, *Nat. Commun.* **2017**, *8*, 705.
[4] Q. H. Wang, K. Kalantar-Zadeh, A. Kis, J. N. Coleman, M. S. Strano, *Nat. Nanotechnol.* **2012**, *7*, 699.
[5] Q. Ma, G. Ren, K. Xu, J. Z. Ou, *Adv. Opt.Mater.* **2021**, *9*, 2001313.
[6] S. Klimmer, O. Ghaebi, Z. Gan, A. George, A. Turchanin, G. Cerullo, G. Soavi, *Nat. Photon.* **2021**, *15*, 837.
[7] A. Autere, H. Jussila, Y. Dai, Y. Wang, H. Lipsanen, Z. Sun, *Adv. Mater.* **2018**, *30*, 1705963.
[8] Z. Sun, A. Martinez, F. Wang, *Nat. Photon.* **2016**, *10*, 227.
[9] H. Mu, S. Lin, Z. Wang, S. Xiao, P. Li, Y. Chen, H. Zhang, H. Bao, S. P. Lau, C. Pan, *Adv. Opt. Mater.* **2015**, *3*, 1447.
[10] J. Chen, Y. Xiong, F. Xu, Y. Lu, *Light: Sci. & Appl.* **2021**, *10*, 78.
[11] A. Abouraddy, M. Bayindir, G. Benoit, S. Hart, K. Kuriki, N. Orf, O. Shapira, F. Sorin, B. Temelkuran, Y. Fink, *Nat. Mater.* **2007**, *6*, 336.
[12] S. Yu, X. Wu, Y. Wang, X. Guo, L. Tong, *Adv. Mater.* **2017**, *29*, 1606128.
[13] X. Zhou, Q. Deng, W. Yu, K. Liu, Z. Liu, *Adv. Funct. Mater.* **2022**, *32*, 2202282.
[14] Q. Bao, H. Zhang, Y. Wang, Z. Ni, Y. Yan, Z. X. Shen, K. P. Loh, D. Y. Tang, *Adv. Funct. Mater.* **2009**, *19*, 3077.
[15] Z. Sun, T. Hasan, F. Torrisi, D. Popa, G. Privitera, F. Wang, F. Bonaccorso, D. M. Basko, A. C. Ferrari, *ACS Nano.* **2010**, *4*, 803.
[16] Y. Li, N. An, Z. Lu, Y. Wang, B. Chang, T. Tan, X. Guo, X. Xu, J. He, H. Xia, *Nat. Commun.* **2022**, *13*, 3138.
[17] Q. Bao, H. Zhang, B. Wang, Z. Ni, C. H. Y. X. Lim, Y. Wang, D. Y. Tang, K. P. Loh, *Nat. Photon.* **2011**, *5*, 411.
[18] E. J. Lee, S. Y. Choi, H. Jeong, N. H. Park, W. Yim, M. H. Kim, J.-K. Park, S. Son, S. Bae, S. J. Kim, *Nat. Commun.* **2015**, *6*, 6851.
[19] T. Ouyang, L. Lin, K. Xia, M. Jiang, Y. Lang, H. Guan, J. Yu, D. Li, G. Chen, W. Zhu, *Opt. Express* **2017**, *25*, 9823.
[20] B. Jiang, Z. Hao, Y. Ji, Y. Hou, R. Yi, D. Mao, X. Gan, J. Zhao, *Light: Sci. & Appl.* **2020**, *9*, 63.
[21] K. Chen, X. Zhou, X. Cheng, R. Qiao, Y. Cheng, C. Liu, Y. Xie, W. Yu, F. Yao, Z. Sun, *Nat. Photon.* **2019**, *13*, 754.
[22] G. Q. Ngo, E. Najafidehaghani, Z. Gan, S. Khazaee, M. P. Siems, A. George, E. P. Schartner, S. Nolte, H. Ebendorff-Heidepriem, T. Pertsch, *Nat. Photon.* **2022**, *16*, 769.
[23] G. Q. Ngo, A. George, R. T. K. Schock, A. Tuniz, E. Najafidehaghani, Z. Gan, N. C. Geib, T. Bucher, H. Knopf, S. Saravi, *Adv. Mater.* **2020**, *32*, 2003826.
[24] J. Xie, X. Cheng, G. Xue, X. Li, D. Zhong, W. Yu, Y. Zuo, C. Liu, K. Lin, C. Liu, *Adv. Mater.* **2024**, *36*, 2403696.
[25] Y. Zuo, W. Yu, C. Liu, X. Cheng, R. Qiao, J. Liang, X. Zhou, J. Wang, M. Wu, Y. Zhao, *Nat. Nanotechnol.* **2020**, *15*, 987.
[26] Y. Yu, Y. Yu, Y. Cai, W. Li, A. Gurarslan, H. Peelaers, D. E. Aspnes, C. G. Van de Walle, N. V. Nguyen, Y.-W. Zhang, *Sci. Rep.* **2015**, *5*, 16996.
[27] Y. V. Morozov, M. Kuno, *Appl. Phys. Lett.* **2015**, 107.
[28] I. Datta, S. H. Chae, G. R. Bhatt, M. A. Tadayon, B. Li, Y. Yu, C. Park, J. Park, L. Cao, D. Basov, *Nat. Photon.* **2020**, *14*, 256.
[29] H.-L. Liu, T. Yang, J.-H. Chen, H.-W. Chen, H. Guo, R. Saito, M.-Y. Li, L.-J. Li, *Sci. Rep.* **2020**, *10*, 15282.
[30] S. Bertolazzi, J. Brivio, A. Kis, *ACS Nano* **2011**, *5*, 9703.
[31] J.-W. Jiang, Z. Qi, H. S. Park, T. Rabczuk, *Nanotechnology* **2013**, *24*, 435705.
[32] H. Li, Q. Zhang, C. C. R. Yap, B. K. Tay, T. H. T. Edwin, A. Olivier, D. Baillargeat, *Adv. Funct. Mater.* **2012**, *22*, 1385.
[33] C. Lee, H. Yan, L. E. Brus, T. F. Heinz, J. Hone, S. Ryu, *ACS Nano* **2010**, *4*, 2695.
[34] Y. Wang, C. Cong, C. Qiu, T. Yu, *Small* **2013**, *9*, 2857.
[35] J.-F. Lin, *Optik* **2010**, *121*, 2144.
[36] K. Yang, A. Zeng, X. Wang, F. Tang, H. Wang, *Chin. Opt. Lett.* **2008**, *6*, 673.